DOI: 10.1002/
Full Paper

Nitrogen-doped hierarchical porous carbon architecture incorporated with cobalt nanoparticles and carbon nanotubes as efficient electrocatalyst for oxygen reduction reaction

Chunyu ZHU[a,b], Cheong KIM[b], Yoshitaka AOKI [a,b], and Hiroki HABAZAKI [a,b],*

Dr. Prof. Chunyu ZHU, MS. Cheong KIM, Dr. Prof. Yoshitaka AOKI, and Dr. Prof. Hiroki HABAZAKI
Division of Applied Chemistry & Frontier Chemistry Center, Faculty of Engineering, Hokkaido University, Sapporo, Hokkaido 060-8628, Japan
Graduate School of Chemical Sciences and Engineering, Hokkaido University, Sapporo, Hokkaido 060-8628, Japan
E-mail address: chunyu6zhu@eng.hokudai.ac.jp (Chunyu Zhu)

Keywords: oxygen reduction reaction, porous carbon, carbon nanotubes, cobalt, combustion synthesis

Hierarchical porous carbon has attracted great interest because of its distinctive structure and superior properties for designing electrochemical energy storage & conversion devices. In this work, we report a novel method to fabricate nitrogen-doped hierarchical porous carbon (NHPC), which is incorporated with Co nanoparticles and carbon nanotubes (CNTs). The NHPC is prepared using a facile and scalable MgO-Co template method. Metal nitrate-glycine solution combustion synthesis (SCS), followed

by a high temperature calcination, is used to prepare MgO-Co/N-doped carbon precursor. CNTs are formed by the in-situ Co-catalytic growth during heat treatment; at the same time, localized graphtic layers are also formed around the Co nanoparticles. After acid washing, NHPC with hierarchical multipores and ultrafine Co nanoparticles is obtained. When applied as ORR catalyst, the NHPC displays high catalytic activity not only in terms of onset potential and current density, but also superior durability and tolerance to methanol crossover in alkaline electrolyte. The remarkable ORR activity is originated from the cooperative effects of high specific surface area, hierarchical pore structure, ultra-small Co nanocrystals, localized graphatic layers, CNTs and N-doping.

1. Introduction

Electrochemical oxygen reduction reaction (ORR) plays critical roles in many energy storage and conversion technologies, including metal-air batteries and fuel cells. To date, platinum (Pt) and Pt-based materials are used for efficient ORR catalysts, however, their wide application have been hindered by the high-cost and scarcity of Pt. Therefore, there is an urgent demand to search high-efficient and nonprecious metal catalysts to reduce the system cost and improve the catalytic stability.[1-2] So far, a number of efforts have been devoted to explore various cost-effective alternatives, such

as spinel/perovskite oxides[3-4], heteroatom (N, S, P et al.) doped carbon[5-10], carbon materials (porous carbon, carbon nanotube (CNT), carbon nanofiber (CNF), graphene/graphene oxide) supported with transition metal/oxides/nitrides/sulfides[11-16] and so on. Among them, transition metal and nitrogen co-doped carbon (M, N-C) electrocatalysts have been dramatically drawn attentions owing to their low-cost and desirable catalytic activity. One of the most efficient strategies to prepare M, N-C electrocatalysts is the direct pyrolysis of appropriate precursors containing nitrogen, carbon and transition metals, such as metal-organic frameworks (MOF), porphyrin polymer, polyimide, and so on. [11, 17-25] Another approach involves the post-treatment of commercially available carbon materials, which usually contains several steps, such as doping/coating with metal precursor and post-annealing under NH_3 gas.[26-29] In spite of these efforts with reported nonprecious metal electrocatalysts which present competitive or even better activity than traditional Pt catalyst, it is still a challenge to prepare high-performance M, N-C electrocatalysts by a facile and scalable method, which employs raw materials of non-expensive, industrially available and low-toxic.

Another consideration for producing a highly active M, N-C electrocatalyst is to introduce accessible catalytic sites as many as possible, which can be achieved by increasing the specific surface area and introducing abundant and suitable pore

structures into the catalyst. A 3D hierarchical porous structure has been regarded as one of the most promising electrocatalysts and electrocatalyst supports. The micropores and mesopores could increase the active sites, and the macropores could promote the mass transport toward and away from the active sites.[19, 30-35] To date, the common routes for fabricating hierarchical carbon structures typically involve templates, such as porous alumina[36-37], silica[31, 38], and zeolite[39], and polystyrene[40]. However, most of the studies use high cost and high toxic starting materials. Additionally, to remove the rigid templates, a highly corrosive alkaline regent or a highly toxic HF solution is often employed. Furthermore, to obtain a desired hierarchical (micro-, meso- and/or macro-) architecture, an additional activation treatment, for example by KOH, is required. All of these will hold back the potential for scaling-up and may also inevitably leach out some active species. Therefore, a facile approach is highly desirable to synthesize hierarchical porous carbon for high-performance ORR catalyst.

In this work, we present a novel, facile and scalable synthesis strategy to fabricate a nitrogen-doped hierarchical porous carbon (NHPC) architecture, which is incorporated with ultrasmall Co nanoparticles, CNTs and locallized graphatic layers, for use as a high-performance ORR catalyst, in which the balance of catalytic active site density, porous structure, specific surface area, and N species play key roles in determining the

ORR performance. The NHPC is prepared using a facile MgO-Co template method. The MgO-Co/N-C precursor is obtained by solution combustion synthesis (SCS, a pre-pyrolysis process) of corresponding metal nitrate-glycine mixture, followed by a high-temperature heat treatment. Glycine is used as the carbon precursor containing N source, which is a very simple and low-cost industry chemical. After removing the template with acid etching, the carbon sample exhibits a hierarchical porous structure consisting macropores, mesopores and micropores. Pore structure is predictable and designable, in which macropores are formed during the SCS process, whereas mesopores and micropores are controlled by the MgO-Co template. Additionally, localized graphitic layers are formed around Co nanoparticles due to the promoted graphitization effect of transition metal. CNTs are formed in-situ with the catalytic assistance of Co nanoparticles during heat treatment.

2. Results and discussion

2.1 Structural and morphology characterization of the precursors

Figure 1 shows the schematic diagram for the preparation process for synthesizing NHPC as-incorporated with Co nanoparticles and CNTs. The NHPC was

prepared by the auto-combustion of nitrate-glycine gels with subsequent heat-treatment and acid washing. The auto-combustion (step 1) of nitrate-glycine gels is the well-known SCS process, which is an exothermic and self-sustaining redox reaction process by heating a mixture of metal nitrates and glycine or other organic fuels. The SCS process has been used to synthesize a variety of useful oxide materials, which shows many advantages such as fast preparation with auto-combustion at low temperature, easy doping of elements with trace amount, and products with nanosized and/or highly porous structure. [41-51] Here, in this study, we employed the glycine-nitrate-based SCS process to produce MgO/N-C and MgO-CoO_x/N-C precursors under Ar atmosphere. $Mg(NO_3)_2$ or a mixture of $Mg(NO_3)_2$ and $Co(NO_3)_2$ were used as both the oxidants for SCS reaction and the raw material to obtain MgO or MgO-Co template for creating a plenty of pores in the final carbon products. Since that the purpose of this study was to produce carbon, an excess amount of glycine was used as the carbon source which contained nitrogen element as dopant to the final carbon product, which is also a very simple and low-cost industry chemical. Due to the foaming feature of the SCS reaction with the emission of a large amount of gases in a short duration, numerous pores in a wide range from several tens of nanometers to several microns were created. Subsequently, the SCSed precursors were carbonized at a

high temperature (step 2). With the addition of cobalt precursor in the raw material, metallic cobalt was easily formed by carbothermal reduction. During the heat treatment, metallic cobalt nanoparticles acted as the catalysts for the in-situ growth of CNTs as-incorporated in the composite matrix. Finally, after being leached with acid solution (step 3), NHPC as-incorporated with CNTs and cobalt nanoparticles can be produced. The characterization of the samples at different stages is shown as following.

During heating-up the nitrate-glycine gels under Ar atmosphere, the SCS reaction was observed near 300 °C, which was featured by the emission of a large amount of gases in a few seconds. At the same time, if a thermocouple was inserted in the reactant to monitor the temperature change, an increasing temperature jump could be observed, indicating a typical self-sustaining exothermic reaction. The SCS reaction with excess amount of glycine fuel under Ar atmosphere was gentle as-compared with those under near stoichiometric conditions and under air atmosphere.[41-42, 50, 52-53] Black and foamy carbonaceous samples were collected, which were further pulverized and heat-treated at 800 ^{o}C or 900 ^{o}C for 2 h under Ar flow. Figure S1 (supporting information) shows the typical X-ray diffraction (XRD) patterns of the samples as-derived from raw materials of different metal nitrates after heat treatment at 800 ^{o}C. The XRD pattern for sample Mg-n3-800 can be indexed to a single MgO phase (JCPDS No: 00-004-0829) with good

crystallinity. However, the peaks for sample MgCo-n3-800 are weak, which can be indexed to a MgO phase (JCPDS No: 00-004-0829) and a metallic Co phase (α-Co, JCPDS No: 01-089-4307). Here, the incorporation of Co with MgO shows an effect on restraining the crystal growth of MgO during heat treatment and making Co nanoparticles disperse in MgO-C matrix, as confirmed by the morphology observation. Figure S2 shows the scanning electron microscopy (SEM) images for the samples after heat treatment at 800 ^{o}C for 2 h. Both samples consist of macroporous particles with irregular shapes with size in the order of several hundreds of nanometers to several tens of microns. Macropores in a wide range of several tens of nanometers to several microns are found to be formed in the particles. These macropores are considered to be formed during the SCS process. At a large magnification, cubic MgO particles in the size of 50–100 nm are observed for sample Mg-n3-800. However, such cubic particles are not confirmed for sample MgCo-n3-800; in contrast, nanoparticles of approximately 10 nm are observed to be embedded in the composite matrix. These 10 nm nanoparticles are Co nanoparticles since the high atomic-number element are contrastingly observed under an SEM view. This is also confirmed by transmission electron microscopy (TEM) observation in Figure S3 (SI). Some nanowires are also observed in sample MgCo-n3-800, which are confirmed to be multi-wall CNTs by further TEM observation.

X-ray energy dispersive spectrometry (EDS) was used to identify the elemental composition of those samples, as shown in Figure S4 (SI), and the composition difference of the Co peaks is confirmed.

2.2 Structural and morphology characterization of the porous carbon

To obtain the final carbon materials, the above MgO/N-C and MgO-Co/N-C composites were leached with HCl solution to remove soluble substances. XRD patterns of the samples are presented in Figure 2 (a). There are two broad peaks at approximately 25 and 43 °, corresponding to the (002) and (100) planes of graphitic carbon, respectively. These patterns of the carbon materials suggest a low graphitization degree. The graphitization degree of sample MgCo-n3-800 is slightly higher than that of Mg-n3-800, as-evidenced by the peak intensity of the (100) plane which is almost invisible for Mg-n3-800. Raman spectroscopy has been widely used to characterize carbon materials and is sensitive to slight changes of C-C bonds of carbon materials.[54-55] As presented in Figure 2 (b), a prominent D-band is located at approximately 1350 cm^{-1}, which is associated with a defective or disordered carbon structure. The typical G-band at approximately 1585 cm^{-1} is related to ordered sp2 bonded graphitic carbon. Generally, the D-band/G-band intensity ratio (I_D/I_G) represents

the disorder degree of carbon materials. The I_D/I_G ratio for Mg-n3-800 carbon is determined to be 1.03, which is higher than the value for MgCo-n3-800 carbon of 0.95. This indicates that MgCo-n3-800 carbon is much more graphitized than the Mg-n3-800 carbon. It has been reported that the incorporation of transition metals, such as Ni, Fe and Co, as catalysts during heat treatment can promote the graphitization process.[56-57]

The properties of the carbon materials were also evaluated using Electron energy loss spectroscopy (EELS), as shown in Figure 2 (c). The spectra reveal two distinct absorption features starting at approximately 275 eV and 400 eV, corresponding to the C-K and N-K edge, respectively. For the C-K edge, the defining π* peak at approximately 280 eV corresponds to the graphitic carbon. The π* peak for the MgCo-n3-800 carbon is stronger and sharper than that for the Mg-n3-800 carbon, indicating the higher graphitic crystallinity of sample MgCo-n3-800. This result is consistent with the Raman and XRD analysis. For the N-K edge, the N peaks are clearly observed for the Mg-n3-800 carbon, whereas these peaks for sample MgCo-n3-800 are indistinct. This indicates that sample Mg-n3-800 contains a higher amount of N than sample MgCo-n3-800, which will be further discussed by X-ray photoelectron spectroscopy (XPS) measurement. As also observed in the EDS spectra (Figure S5)

under SEM observation, the N-peak is observed for the Mg-n3-800 carbon, whereas the N-peak for MgCo-n3-800 is indistinct.

The functional groups and bonding characteristics of the samples were further performed on XPS. As shown in Figure 2 (d), the survey XPS spectra of the carbon samples display three peaks at 285.1, 399.3 and 534.2 eV, corresponding to C 1s, N 1s and O 1s, respectively. Both samples contain nitrogen, and the atomic percentage of N in the carbon samples are about 16.5 and 3.5 atom% for Mg-n3-800 and MgCo-n3-800, respectively. The high-resolution N 1s spectra can be divided into three individual peaks, representing the pyridinic N (~398.5 eV), pyrrolic or pyridonic N (~400.2 eV), quaternary N (graphitic N, ~401.2 eV). [58-59] The N binding configuration for sample Mg-n3-800 includes 45.9% pyridinic N, 45.6% pyrrolic N, and 8.5% quaternary N, respectively. These values for sample MgCo-n3-800 are 41.8%, 25.1%, and 33.1%, respectively. The results are summarized in Table 1. The content of the graphitic N for sample MgCo-n3-800 is higher than sample Mg-n3-800, which is due to the catalytic graphitization effect of Co, introducing a better electrical conductivity of the referred carbon sample. Pyridinic N and quaternary N are the majority for sample MgCo-n3-800, which is favorable for enhancing the ORR performance because these two types of N species are usually considered to be active sites for ORR. [60-62]

The specific surface area and pore size distribution of the carbon materials were measured by a nitrogen adsorption-desorption experiment. Figure 3 (a) shows the nitrogen sorption isotherms, which illustrate the typical type-IV curves with obvious hysteresis loops, indicating the coexisting of micropores, mesopores and macropores. Here, the strong nitrogen adsorption at relative pressure less than 0.1 represents the presence of micropores. The obvious hysteresis loop between the adsorption and desorption branches at ~0.5–0.9 P/P_0 indicates the existence of mesopores. The steep adsorption at relative pressure of ~0.9–1.0 demonstrates the presence of macropores. The specific surface areas, as-evaluated by Brunauer-Emmett-Teller (BET) method, are 454 and 1230 m^2 g^{-1} for samples Mg-n3-800 and MgCo-n3-800, respectively. The Barrett–Joyner–Halenda (BJH) pore size distributions of the samples are shown in Figure 3 (b). The samples present mesopores with most of their diameters less than ~10 nm. The peak mesopore diameters locate at ~2.44 nm, and the average ones are in the range of ~4–5 nm. The total pore volume (V_{total}), as-determined from the amount of nitrogen adsorbed at the relative pressure (P/P_0) of 0.9, are 0.35 and 1.01 cm^3 g^{-1} for samples Mg-n3-800 and MgCo-n3-800, respectively. The specific surface areas, including S_{total}, $S_{external}$ and S_{micro}, and micropore volume were also analyzed by *t* method. The summarized results are shown in Table 2. The micropore volumes are 0.23

and 0.61 cm^3 g^{-1} for Mg-n3-800 and MgCo-n3-800, respectively. It is concluded from the above results that, with the addition of Co, the obtained carbon present higher specific surface area and pore volume. The above structural parameters for the porous carbon are summarized in Table 2.

Figure 4 presents the SEM micrographs for carbon products Mg-n3-800 and MgCo-n3-800. More SEM images are also presented in Figure S6. Both samples comprise irregular bulk shapes in the order of several hundreds of nanometers to several tens of microns. Macropores of several tens of nanometers to several microns are found in the bulk materials, and the as-prepared carbon materials have a loose structure. As described previously, these macropores are considered to be formed in the SCS process due to the emission of a large amount of gases. As observed in the SEM image at a large magnification, sample MgCo-n3-800 contains a few nanowires that extrude from the porous carbon matrix. These nanowires are confirmed to be multi-wall CNTs based on TEM examination.

The morphology and structure of the carbon samples were further carefully examined using TEM. Figure 5 (a) presents a typical TEM image for the overview of the obtained carbon at a low magnification and a highly porous structure is confirmed. Figure 5 (b) shows the selected area electron diffraction (SAED) pattern of the carbon

materials, which indicates a typical amorphous graphite structure. Note that the low-magnification TEM images and SAED patterns for both samples are similar. Sample MgCo-n3-800 was further examined using a Scanning Transmission Electron Microscopy (STEM) detector, as shown in Figures 5 (c) and (d) at various magnifications. Here, the contrast of the bright-filed STEM images is strongly dependent on the average atomic number of the scatterer encountered by the incident probe. Notably, cobalt nanoparticles with size around 1 nm are highly dispersed in the porous carbon matrix. EDS analysis obtained both under SEM and TEM observation (Figures S5 and S7 (SI)) shows that the MgCo-n3-800 carbon processes a small amount of cobalt (less than 1 mass%). Here, the original cobalt nanoparticles of ~10 nm were etched by acid solution, and their size were reduced to ~ 1 nm. The nanowires that grow from the porous carbon matrix are confirmed to be CNTs. Figures 5 (e) and (g) present the high-resolution TEM images of the CNTs at various magnifications. The CNTs have diameters of several nanometers with multi-walls of graphene fringes. The incorporation of CNTs can form a high conductive network for the fast transport of ions and electrons, so as to increase the ORR performance. Figure 5 (f) presents the enlarged high-resolution TEM image of a typical crystallized nanoparticle as embedded in the carbon matrix, revealing an interplanar space of approximately 0.21 nm, which can be

indexed to the (1, 1, 1) plane of metallic cobalt (α-Co, JCPDS No: 01-089-4307). Figures 5 (h) and (i) show the typical high-resolution TEM images of the incorporated metallic cobalt nanoparticles in the porous carbon matrix. Interestingly, graphatic layers around the etched cobalt nanoparticles can be found. The graphitic layers are considered to be formed by the localized graphitization effect of metallic Co. Such stabilized ultrafine Co nanoparticles as-confined in graphitized N-doped carbon shells can provide sufficient active sites besides the C-N active sites.[63-64] The core-shell structure with void between the core of ultrafine Co nanoparticle and the shell of a few graphene layers also allow the easy access to the active sites. Additionally, a typical high-resolution TEM image for the amorphous porous carbon matrix is shown in Figure 5 (j), which represents multi-pores of several nanometers. It is noted that the features of CNTs, cobalt nanoparticles and localized graphitic layers were not observed in sample Mg-n3-800.

The use of cobalt in the raw material is essential for the growth of CNTs during heat treatment. In order to confirm the growth process for CNTs, we also performed the following experiments. First, we examined the morphology of the sample after pre-pyrolysis at 500 ^{o}C, and we found that CNTs were not formed at this temperature. Second, the formation of MgO and Co was observed in the samples after pre-pyrolysis

and sintering at 800 ^{o}C. Third, we performed the thermogravimetric analysis of a pre-pyrolyzed $Co(NO_3)_2$-glycine mixture under Ar flow, which had reactants of CoO_x and carbonaceous materials, and we observed that CoO_x was carbothermally reduced to metallic cobalt at temperature higher than ~500 ^{o}C. Therefore, the formation of CNTs proceeded with the cobalt catalytic growth at higher temperatures, which have been also observed in several literatures.[65-66] A proposed growth mechanism for the formation of the CNT- and Co-incorporated porous carbon is illustrated in Figure 1. A lot of micro- and mesopores were also created by the removal of the homogeneously distributed MgO or MgO-Co nanocrystals in the carbon matrix.

The above characterization and discussion focused on samples Mg-n3-800 and MgCo-n3-800 to confirm the effect of the addition of Co on the as-prepared carbon. Other synthesis parameters including glycine ratio and sintering temperature were also analyzed by preparing samples MgCo-n2.5-800, MgCo-n4-800, and MgCo-n3-900. It is noted that the morphology and structure properties for these three samples are quite similar to sample MgCo-n3-800 as-observed by XRD, SEM and TEM. The through differences, such as specific surface area and nitrogen bonding, of the obtained carbon samples are summarized in Figures S8, S9, S10, S11 and Tables 1, 2.

2.3 Electrochemical performance

The electrochemical properties of the obtained NHPC samples were evaluated in alkaline (0.1 M KOH) solution using rotating disk electrode (RDE). For ORR, the NHPC with hierarchical pore structure and high surface area is expected to have high activity, which allows easy access to active sites and rapid mass transfer processes. The ORR activity was firstly measured by cyclic voltammetry (CV) in both Ar and O_2 saturated KOH electrolyte at a scan rate of 50 mV s^{-1}, as shown in Figure 6 (a). In Ar saturated electrolyte, the samples including commercial Pt/C display featureless slopes and no redox peaks are found in the scanned range. However, a well-defined ORR peak centering at 0.81 V vs RHE is found for sample MgCo-n3-800 in O_2 saturated solution, which is comparable to that of Pt/C (0.84 V) and much higher than that of sample Mg-n3-800 (0.58 V), suggesting a good ORR electrocatalytic activity for sample MgCo-n3-800. To further investigate the ORR reaction kinetics, RDE measurements were also conducted at different rotating speeds. Figure 6 (b) shows the linear sweep voltammetry (LSV) curves for sample MgCo-n3-800 at rotating speeds ranging from 400 to 1600 rpm. Based on the Koutecky–Levich (K-L) plots as presented in Figure 6 (c), a direct four-electron transfer pathway is confirmed. Figure 6 (d) shows the comparison of the LSV curves between samples MgCo-n3-800, Mg-n3-800 and Pt/C at

a rotating speed of 1600 rpm. The onset potential of sample MgCo-n3-800 (0.97 V) is very similar to that of Pt/C (1.01 V), which is greatly higher than that of sample Mg-n3-800 (0.77 V). The half-potential ($E_{1/2}$) and diffusion-limited current density for sample MgCo-n3-800 are 0.86 V and -5.44 mA cm^{-2} respectively, which are quite similar to those for Pt/C (0.84 V and -5.52 mA cm^{-2}) but greatly higher than those for sample Mg-n3-800 (0.58 V and -3.54 mA cm^{-2}). These results indicate the importance of Co and CNT incorporation to the N-doped porous carbon on its enhanced activity toward ORR.

The calcination temperature and glycine ratio are also important synthesis parameters for the Co-incorporated samples. Figure 6 (e) shows the catalytic performance of the samples prepared at different calcination temperature and glycine ratio using RDE experiments at 1600 rpm. Sample MgCo-n3-800 displays the best ORR catalytic activity amongst these samples. The ORR activity for sample MgCo-n3-900 as-calcined at 900 ºC is lower than the sample obtained at 800 ºC, which is due to the decreased amount of N-doping at a higher calcination temperature (see Table 1). For the samples obtained at different glycine ratio from n2.5 to n4 and calcined at 800 ºC, sample MgCo-n4-800 shows the poorest ORR activity which is due to its lowest specific surface area. Sample MgCo-n2.5-800 displays a slightly lower activity than

sample MgCo-n3-800, which is considered to be caused by its slightly lower ratios of N amount.

The stability of sample MgCo-n3-800 and commercial Pt/C catalysts were evaluated by chronoamperometry at -0.4 V vs. Ag/AgCl in O_2-saturated KOH solution at a rotation speed of 1600 rpm, as shown in Figure 7 (a). The current density for sample MgCo-n3-800 almost remains constant during the long-time holding test. However, commercial Pt/C loses 16% of its original current density. This result indicates that our material shows higher stability than Pt/C material.

Additionally, for commercialization, an ideal ORR catalyst should be able to afford the crossover of small-molecule fuels, such as methanol, from anode to cathode, since these small-molecules can penetrate through the polymer electrolyte membrane easily, which may decrease the entire cell efficiency.[29, 38] The methanol tolerance property was measured for sample MgCo-n3-800 in comparison with commercial Pt/C catalyst, as shown in Figure 7 (b). The chronoamperometric responses of the catalysts to the addition of 2 volume% methanol at -0.4 V vs. Ag/AgCl in O_2-saturated KOH solution were recorded. Pt/C exhibits an apparent current shift immediately after the injection of methanol, while no obvious change is observed for sample MgCo-n3-800. The superior

tolerance to methanol crossover effect of sample MgCo-n3-800 further confirms it as a promising cathode catalyst for alkaline direct methanol fuel cells.

The superior electrochemical catalytic performance of the CNT- & Co-incorporated NHPC (MgCo-n3-800) can be explained by its novel hierarchical nanostructure, as presented in Figure 1. Firstly, the abundant pyridinic N and quaternary N-doped carbon provides a large number of N-C active sites.[17, 32, 67] At the same time, the stabilized ultrafine Co nanoparticles as-confined in graphitized N-doped carbon shells can provide additional active sites.[63-64] Such core-shell structure with void between the core of ultrafine Co nanoparticle and the shell of a few graphene layers not only allow the easy access to the active sites, but also prevent the unwanted agglomeration of active sites. Secondly, the high specific surface area and hierarchical porous structure of interconnected macro, meso and micropores, can enhance the penetrability of electrolytes into the interior surfaces, provide efficient electrolyte/mass contact and facilitate fast ion transportation. Furthermore, the open and interconnected pore structure with homogeneously distributed Co, N species can increase the number of exposed active sites and prevent unwanted agglomeration of active sites, which greatly contribute to the enhancement of electrocatalytic activity and stability. Thirdly, the simultaneous incorporation of CNTs and Co nanoparticles can form a 3D percolated

network for the fast transport of ions and electrons. [68-73] Moreover, the CNT-incorporated porous structure is also mechanically strong, avoiding the collapse of electrode structure and agglomeration of active sites.

As beneficial from the synergistic effects of hierarchical pore structure, ultra-small Co nanocrystals, localized graphitic layers, CNTs and N-doping, the NHPC demonstrated high ORR activity, excellent durability and superior tolerance to methanol crossover. Finally, the electrochemical performance of the NHPC is also comparable to that of the best carbon-based ORR catalysts as reported, [9, 31, 37, 63-64, 74-75] indicating its possibility as a promising substitute to commercial Pt/C.

3. Conclusions

NHPC incorporated with CNTs and Co nanoparticles was synthesized using a SCS-initiated MgO-Co template method. The MgO-Co/N-C precursor was prepared by a facile and scalable nitrate-glycine SCS with subsequent calcination. After acid washing, NHPC with high specific surface area was obtained, which also contained macro, meso and micropores. The macropores were formed during the SCS process, whereas the meso and micropores were created by removing the MgO-Co template.

CNTs were formed by in-situ Co-catalytic growth during calcination. Additionally, localized graphitic layers were also formed around the Co nanoparticles. Because of the synergistic effect of high specific surface area, interconnected macro, meso and micropores, nitrogen-doping, localized graphitic layers, and incorporation of Co nanoparticles and CNTs, the NHPC demonstrated high activity, excellent durability and superior tolerance to ethanol crossover as a ORR catalyst, which was comparable to commercial Pt/C. Moreover, the obtained NHPC can also be applied in Li/Na ion batteries, supercapacitors, and adsorbents due to its unique structure.

4. Experimental section

Synthesis of porous carbon: In the experiment, metal nitrates (5 mmol $Mg(NO_3)_2 \cdot 6H_2O$ or 4 mmol $Mg(NO_3)_2 \cdot 6H_2O$ and 1 mmol $Co(NO_3)_2 \cdot 6H_2O$) and glycine (NH_2CH_2COOH, 12.5, 15, or 20 mmol) were dissolved in 5 ml distilled water to form homogenous solutions under magnetic stirring. Subsequently, the solutions were evaporated on a hot plate with magnetic stirring to form dried gels. The obtained gels were heated to 500 ^oC at a temperature ramp of 10 ^oC min^{-1} under Ar flow to preliminarily pyrolyze the nitrates and organic material. Subsequently, the pyrolyzed

samples were roughly pulverized using a mortar and pestle. The samples were then heated to 800 ^{o}C or 900 ^{o}C at a temperature ramp of 10 ^{o}C min^{-1} and kept at this temperature for 2 h under Ar flow. Finally, the calcined samples were leached with 0.2 M HCl solution for 24 h, filtered, washed with distilled water and ethanol for several times, and dried to obtain porous carbon materials. Five samples were prepared, which were named based on the as-used metal nitrates (Mg or MgCo), the ratio of glycine to nitrate (n2.5, n3 and n4), and calcination temperature (800 ^{o}C and 900 ^{o}C). These samples were Mg-n3-800, MgCo-n2.5-800, MgCo-n3-800, MgCo-n4-800, and MgCo-n3-900.

Material characterization: The samples were characterized by X-ray diffraction (XRD, Rigaku Miniflex, CuKα), transmission electron microscopy (TEM, 200 kV, JEM-2010F), and scanning electron microscopy (SEM, JEOL, JSM-7400F) combined with an X-ray energy dispersive spectrometry (EDS) for their crystalline structure, morphology and elemental composition analysis. Electron energy loss spectroscopy (EELS) combined with the TEM observation was also used to analyze the properties of the carbon materials. Surface functional groups and bonding characterization of the samples were performed on X-ray photoelectron spectroscopy (XPS, JEOL, JPS-9200) system using a Mg-Kα X-ray source. Raman spectra of the samples were acquired using

a RENISHAW Raman spectrometer using an excitation wavelength of 532 nm. The Brunauer-Emmett-Teller (BET) specific surface area and pore size distribution of the samples were characterized by nitrogen sorption using a BELSORP-mini surface area analyzer.

Electrochemical measurement: Electrochemical measurements were carried out in a typical three-electrode system on a Princeton electrochemical workstation, with a saturated Ag/AgCl reference electrode and a platinum plate counter electrode and a rotating disk electrode (RDE) as working electrode. The catalyst suspension was prepared as follows: 5.0 mg carbon catalyst or commercial Pt/C (20 wt%-Pt, Sigma Aldrich) was dispersed in 1 mL ethanol with the addition of 40 μL 5% Nafion solution, which was ultrasonic agitated for at least 30 minutes. The working electrode was prepared by dropping 6 μL of the above catalyst ink on a polished glassy carbon electrode (GCE, with a geometric surface area of 0.196 cm^2) and drying it at room temperature. The electrolyte was a 0.1 M KOH solution, which was saturated with Ar/O_2 by bubbling Ar/O_2 for at least 30 min before measurement. The ORR performance was investigated by linear sweep voltammetry (LSV) at a scan rate of 10 mV s^{-1} with various rotating speed from 400 rpm to 1600 rpm in the O_2 saturated

electrolyte. Cyclic voltammetry (CV) was carried out at a scan rate of 50 mV s^{-1} in both Ar and O_2 bubbled electrolyte.

All experimental results for the ORR activity in this paper were reported as current density versus applied potential (vs. RHE), and the current density was normalized using geometric surface area of a glassy carbon electrode with 5 mm diameter. The measured potentials were converted to the reversible hydrogen electrode (RHE) via the Nernst equation:

$$E_{RHE} = E_{Ag/AgCl} + 0.059pH + E_{0Ag/AgCl} \quad (1)$$

where E_{RHE} is the converted potential versus RHE, $E_{Ag/AgCl}$ is the experimental potential measured against the Ag/AgCl reference electrode, and $E_{0Ag/AgCl}$ is the standard potential of Ag/AgCl at 25 ^{o}C (0.197 V). The pH is 13 for the used electrolyte of 0.1 M KOH.

The overall electron transfer numbers per oxygen molecule involved in the typical ORR process were calculated from the slopes of the Koutecky–Levich (K-L) plots using the following equations:

$$\frac{1}{j} = \frac{1}{j_L} + \frac{1}{j_K} = \frac{1}{B\omega^{1/2}} + \frac{1}{j_K} \quad (2)$$

$$B = 0.62nFC_0D_0^{2/3}v^{-1/6} \quad (3)$$

$$j_K = nFkC_0 \quad (4)$$

where j is the measured current density, j_L and j_K are the diffusion-limiting and kinetic current densities (mA/cm^2), respectively. n represents the overall number of electrons gained per O_2, F is the Faraday constant (F = 96485 C mol^{-1} = 96485000 mA s mol^{-1}), C_0 is the bulk concentration of O_2 (1.2 × 10^{-6} mol cm^{-3}), D_0 is the diffusion coefficient of O_2 in 0.1 M KOH electrolyte (1.9 × 10^{-5} cm^2 s^{-1}), v is the kinetic viscosity of the electrolyte (0.01 cm^2 s^{-1}), ω is the angular velocity of the disk (rad/s) ($\omega = 2\pi N$, N is the linear rotation speed at rotation per second) and k is the electron transfer rate constant.

Supporting Information

Supporting Information is available from the Wiley Online Library or from the author.

Acknowledgements

This work is supported partially by Nippon Sheet Glass Foundation for Materials Science and Engineering and JSPS KAKENHI. The authors also thank Dr. G. Saito for his help on TEM observation.

References

[1] D.-W. Wang, D. Su, *Energy & Environmental Science* **2014**, *7*, 576-591.

[2] M. K. Debe, *Nature* **2012**, *486*, 43-51.

[3] P. Li, R. Ma, Y. Zhou, Y. Chen, Z. Zhou, G. Liu, Q. Liu, G. Peng, Z. Liang, J. Wang, *Journal of Materials Chemistry A* **2015**, *3*, 15598-15606.

[4] I. Yamada, H. Fujii, A. Takamatsu, H. Ikeno, K. Wada, H. Tsukasaki, S. Kawaguchi, S. Mori, S. Yagi, *Advanced Materials* **2017**, *29*, 1603004-n/a.

[5] Y. Liu, Y. Shen, L. Sun, J. Li, C. Liu, W. Ren, F. Li, L. Gao, J. Chen, F. Liu, Y. Sun, N. Tang, H.-M. Cheng, Y. Du, *Nat Commun* **2016**, *7*, 10921.

[6] R. Sharma, K. K. Kar, *Electrochimica Acta* **2016**, *191*, 876-886.

[7] V. Perazzolo, E. Grądzka, C. Durante, R. Pilot, N. Vicentini, G. A. Rizzi, G. Granozzi, A. Gennaro, *Electrochimica Acta* **2016**, *197*, 251-262.

[8] B. You, P. Yin, J. Zhang, D. He, G. Chen, F. Kang, H. Wang, Z. Deng, Y. Li, *Sci. Rep.* **2015**, *5*, 11739.

[9] Y. Zhang, X. Zhang, X. Ma, W. Guo, C. Wang, T. Asefa, X. He, *Scientific Reports* **2017**, *7*, 43366.

[10] Y. Chen, R. Ma, Z. Zhou, G. Liu, Y. Zhou, Q. Liu, S. Kaskel, J. Wang, *Advanced Materials Interfaces* **2015**, *2*, 1500199-n/a.

[11] S. Bruller, H.-W. Liang, U. I. Kramm, J. W. Krumpfer, X. Feng, K. Mullen, *Journal of Materials Chemistry A* **2015**, *3*, 23799-23808.

[12] G. Zhang, B. Y. Xia, X. Wang, X. W. Lou, *Advanced Materials* **2014**, *26*, 2408-2412.

[13] J. Pandey, B. Hua, W. Ng, Y. Yang, K. van der Veen, J. Chen, N. J. Geels, J.-L. Luo, G. Rothenberg, N. Yan, *Green Chemistry* **2017**.

[14] X. Zhao, Y. Li, Y. Guo, Y. Chen, Z. Su, P. Zhang, *Advanced Materials Interfaces* **2016**, *3*, 1600658-n/a.

[15] L. Liu, Y. Hou, J. Wang, J. Chen, H.-K. Liu, Y. Wu, J. Wang, *Advanced Materials Interfaces* **2016**, *3*, 1600030-n/a.

[16] X. Liu, I. S. Amiinu, S. Liu, Z. Pu, W. Li, B. Ye, D. Tan, S. Mu, *Advanced Materials Interfaces* **2017**, 1601227-n/a.

[17] Y. Pei, Z. Qi, X. Li, R. V. Maligal-Ganesh, T. W. Goh, C. Xiao, T. Wang, W. Huang, *Journal of Materials Chemistry A* **2017**, *5*, 6186-6192.

[18] Q. Lin, X. Bu, A. Kong, C. Mao, F. Bu, P. Feng, *Advanced Materials* **2015**, *27*, 3431-3436.

[19] Y. Cao, Y. Ma, T. Wang, X. Wang, Q. Huo, Y. Liu, *Crystal Growth & Design* **2016**, *16*, 504-510.

[20] G. Wu, K. L. More, C. M. Johnston, P. Zelenay, *Science* **2011**, *332*, 443-447.

[21] M. Rafti, W. A. Marmisollé, O. Azzaroni, *Advanced Materials Interfaces* **2016**, *3*, 1600047-n/a.

[22] G. Lu, Y. Zhu, L. Lu, K. Xu, H. Wang, Y. Jin, Z. Jason Ren, Z. Liu, W. Zhang, *Journal of Power Sources* **2016**, *315*, 302-307.

[23] G. Lu, H. Yang, Y. Zhu, T. Huggins, Z. J. Ren, Z. Liu, W. Zhang, *Journal of Materials Chemistry A* **2015**, *3*, 4954-4959.

[24] Z. Xiang, D. Cao, L. Huang, J. Shui, M. Wang, L. Dai, *Advanced Materials* **2014**, *26*, 3315-3320.

[25] G. Lu, Y. Zhu, K. Xu, Y. Jin, Z. J. Ren, Z. Liu, W. Zhang, *Nanoscale* **2015**, *7*, 18271-18277.

[26] C. Domínguez, F. J. Pérez-Alonso, M. Abdel Salam, J. L. Gómez de la Fuente, S. A. Al-Thabaiti, S. N. Basahel, M. A. Peña, J. L. G. Fierro, S. Rojas, *International Journal of Hydrogen Energy* **2014**, *39*, 5309-5318.

[27] X.-J. Huang, Y.-G. Tang, L.-F. Yang, P. Chen, Q.-S. Wu, Z. Pan, *Journal of Materials Chemistry A* **2015**, *3*, 2978-2984.

[28] Q. Huang, P. Zhou, H. Yang, L. Zhu, H. Wu, *Electrochimica Acta* **2017**, *232*, 339-347.

[29] J. Li, Y. Song, G. Zhang, H. Liu, Y. Wang, S. Sun, X. Guo, *Advanced Functional Materials* **2017**, *27*, 1604356-n/a.

[30] F.-L. Meng, Z.-L. Wang, H.-X. Zhong, J. Wang, J.-M. Yan, X.-B. Zhang, *Advanced Materials* **2016**, *28*, 7948-7955.

[31] Z. Pei, H. Li, Y. Huang, Q. Xue, Y. Huang, M. Zhu, Z. Wang, C. Zhi, *Energy & Environmental Science* **2017**, *10*, 742-749.

[32] G. Wang, Y. Sun, D. Li, H.-W. Liang, R. Dong, X. Feng, K. Müllen, *Angewandte Chemie* **2015**, *127*, 15406-15411.

[33] M. Wu, J. Qiao, K. Li, X. Zhou, Y. Liu, J. Zhang, *Green Chemistry* **2016**, *18*, 2699-2709.

[34] W. Zhang, Y. Fu, J. Wang, X. Wang, *Advanced Materials Interfaces* **2017**, 1601219-n/a.

[35] Y. An, Z. Li, Y. Yang, B. Guo, Z. Zhang, H. Wu, Z. Hu, *Advanced Materials Interfaces* **2017**, 1700033-n/a.

[36] E. Tsuji, T. Yamasaki, Y. Aoki, S.-G. Park, K.-i. Shimizu, H. Habazaki, *Carbon* **2015**, *87*, 1-9.

[37] X. Zhao, F. Li, R. Wang, J.-M. Seo, H.-J. Choi, S.-M. Jung, J. Mahmood, I.-Y. Jeon, J.-B. Baek, *Advanced Functional Materials* **2017**, *27*, 1605717.

[38] L. Shang, H. Yu, X. Huang, T. Bian, R. Shi, Y. Zhao, G. I. N. Waterhouse, L.-Z. Wu, C.-H. Tung, T. Zhang, *Advanced Materials* **2016**, *28*, 1668-1674.

[39] Y. Kwon, K. Kim, R. Ryoo, *RSC Advances* **2016**, *6*, 43091-43097.

[40] J. Liang, R. F. Zhou, X. M. Chen, Y. H. Tang, S. Z. Qiao, *Advanced Materials* **2014**, *26*, 6074-6079.

[41] C. Zhu, A. Nobuta, I. Nakatsugawa, T. Akiyama, *International Journal of Hydrogen Energy* **2013**, *38*, 13238-13248.

[42] C. Zhu, T. Akiyama, *Electrochimica Acta* **2014**, *127*, 290-298.

[43] M. J. Wilcox, L. J. Groven, *International Journal of Hydrogen Energy* **2017**, *42*, 6765-6770.

[44] P. S. Barbato, S. Colussi, A. Di Benedetto, G. Landi, L. Lisi, J. Llorca, A. Trovarelli, *The Journal of Physical Chemistry C* **2016**, *120*, 13039-13048.

[45] A. Varma, A. S. Mukasyan, A. S. Rogachev, K. V. Manukyan, *Chemical Reviews* **2016**.

[46] W. Wen, J.-M. Wu, *RSC Advances* **2014**, *4*, 58090-58100.

[47] C.-G. Han, C. Zhu, G. Saito, T. Akiyama, *Electrochimica Acta* **2016**, *209*, 225-234.

[48] C.-G. Han, C. Zhu, N. Sheng, Y. Aoki, H. Habazaki, T. Akiyama, *Electrochimica*

Acta **2017**, *235*, 88-97.

[49] C. Zhu, C.-g. Han, G. Saito, T. Akiyama, *RSC Advances* **2016**, *6*, 30445-30453.

[50] C. Zhu, A. Nobuta, Y.-W. Ju, T. Ishihara, T. Akiyama, *International Journal of Hydrogen Energy* **2013**, *38*, 13419-13426.

[51] C. Zhu, G. Saito, T. Akiyama, *Journal of Alloys and Compounds* **2015**, *633*, 424-429.

[52] C. Zhu, A. Nobuta, G. Saito, I. Nakatsugawa, T. Akiyama, *Advanced Powder Technology* **2014**, *25*, 342-347.

[53] C. Zhu, C.-g. Han, T. Akiyama, *RSC Advances* **2015**, *5*, 49831-49837.

[54] P. Dornath, S. Ruzycky, S. Pang, L. He, P. Dauenhauer, W. Fan, *Green Chemistry* **2016**, *18*, 6637-6647.

[55] X. Liu, I. S. Amiinu, S. Liu, K. Cheng, S. Mu, *Nanoscale* **2016**, *8*, 13311-13320.

[56] Y. Chen, X. Li, X. Zhou, H. Yao, H. Huang, Y.-W. Mai, L. Zhou, *Energy & Environmental Science* **2014**, *7*, 2689-2696.

[57] B. Zhang, Z.-L. Xu, Y.-B. He, S. Abouali, M. Akbari Garakani, E. Kamali Heidari, F. Kang, J.-K. Kim, *Nano Energy* **2014**, *4*, 88-96.

[58] J. Ou, Y. Zhang, L. Chen, Q. Zhao, Y. Meng, Y. Guo, D. Xiao, *Journal of Materials Chemistry A* **2015**, *3*, 6534-6541.

[59] L. Chen, Y. Zhang, C. Lin, W. Yang, Y. Meng, Y. Guo, M. Li, D. Xiao, *Journal of Materials Chemistry A* **2014**, *2*, 9684-9690.

[60] J. Wei, Y. Liang, X. Zhang, G. P. Simon, D. Zhao, J. Zhang, S. Jiang, H. Wang, *Nanoscale* **2015**, *7*, 6247-6254.

[61] J. Chen, X. Wang, X. Cui, G. Yang, W. Zheng, *Chemical Communications* **2014**, *50*, 557-559.

[62] H. Yu, L. Shang, T. Bian, R. Shi, G. I. N. Waterhouse, Y. Zhao, C. Zhou, L.-Z. Wu, C.-H. Tung, T. Zhang, *Advanced Materials* **2016**, *28*, 5080-5086.

[63] S. H. Ahn, A. Manthiram, *Small* **2017**, *13*, 1603437.

[64] F. Hu, H. Yang, C. Wang, Y. Zhang, H. Lu, Q. Wang, *Small* **2017**, *13*, 1602507.

[65] B. Y. Xia, Y. Yan, N. Li, H. B. Wu, X. W. Lou, X. Wang, **2016**, *1*, 15006.

[66] G. Zhang, W. Lu, F. Cao, Z. Xiao, X. Zheng, *Journal of Power Sources* **2016**, *302*, 114-125.

[67] J. Shui, C. Chen, L. Grabstanowicz, D. Zhao, D.-J. Liu, *Proceedings of the National Academy of Sciences* **2015**, *112*, 10629–10634.

[68] G. Pandey, A. Biswas, *Computational Materials Science* **2014**, *89*, 80-88.

[69] K. Choi, C. Yu, *PloS one* **2012**, *7*, e44977.

[70] H. Palza, C. Garzón, O. Arias, *Express Polymer Letters* **2012**, *6*, 639-646.

[71] T. Nomura, C. Zhu, S. Nan, K. Tabuchi, S. Wang, T. Akiyama, *Applied Energy* **2016**, *179*, 1-6.

[72] T. Nomura, K. Tabuchi, C. Zhu, N. Sheng, S. Wang, T. Akiyama, *Applied Energy* **2015**, *154*, 678-685.

[73] C. Zhu, T. Akiyama, *Green Chemistry* **2016**, *18*, 2106-2114.

[74] P. K. Sonkar, K. Prakash, M. Yadav, V. Ganesan, M. Sankar, R. Gupta, D. K. Yadav, *Journal of Materials Chemistry A* **2017**, *5*, 6263-6276.

[75] D. K. Singh, R. N. Jenjeti, S. Sampath, M. Eswaramoorthy, *Journal of Materials Chemistry A* **2017**, *5*, 6025-6031.

Table 1. Summary of composition properties of the porous carbon from XPS analysis

Sample	C atom%	O atom%	N atom%	Quaternary N atom%	Pyrrolic N atom%	Pyridinic N atom%
Mg-n3-800	*75.2*	*8.3*	*16.5*	*8.5*	*45.6*	*45.9*
MgCo-n2.5-800	92.7	4.1	3.2	34.2	29.0	36.8
MgCo-n3-800	*92.1*	*4.4*	*3.5*	*33.1*	*25.1*	*41.8*
MgCo-n4-800	90.2	5.8	4.0	23.1	35.0	41.9
MgCo-n3-900	94.3	4.4	1.3	42.0	26.1	31.9

Table 2. Structural parameters of the porous carbon from BET N_2 sorption measurement

Sample	V_{total}	*BET analysis*			*t method analysis*				
	[$cm^3\ g^{-1}$]	S_{BET} [$m^2\ g^{-1}$]	$D_{average}$ [nm]	$D_{peak,\ meso}$ [nm]	S_{total} [$m^2\ g^{-1}$]	$S_{external}$ [$m^2\ g^{-1}$]	S_{micro} [$m^2\ g^{-1}$]	V_{micro} [$cm^3\ g^{-1}$]	V_{meso} [$cm^3\ g^{-1}$]
Mg-n3-800	*0.35*	*454*	*5.09*	*2.44*	*452*	*107*	*345*	*0.23*	*0.12*
MgCo-n2.5-800	1.14	1200	5.82	2.44	1172	548	624	0.53	0.61
MgCo-n3-800	*1.01*	*1230*	*4.22*	*2.44*	*1244*	*364*	*880*	*0.61*	*0.40*
MgCo-n4-800	0.47	720	2.94	2.44	819	109	710	0.37	0.10
MgCo-n3-900	1.03	1110	6.29	3.33	1143	380	763	0.60	0.43

V_{total}: total pore volume at P/P_0=0.9; S_{BET}: specific surface area as-calculated from the adsorption data by BET method; $D_{average}$: average pore diameter as-determined by BET method; $D_{peak,\ meso}$: peak meso-pore diameter as-determined by BJH model; S_{total}: the total surface area as-determined by t method; $S_{external}$: the external surface area as-determined by t method; S_{micro}: the micropore surface area as-determined by S_{total}-$S_{external}$; V_{micro}: the micropore volume as-analyzed by *t* method; V_{meso}: the mesopore volume as-determined by V_{total}-V_{micro}.

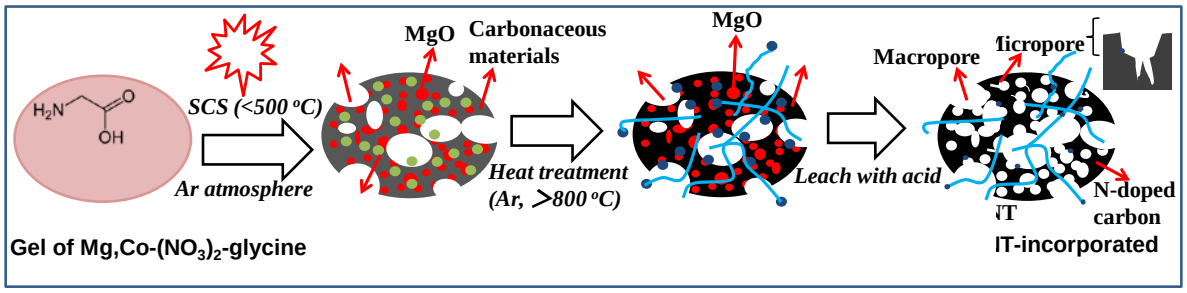

Figure 1. Schematic diagram for the formation process of the NHPC as incorporated with CNTs and cobalt nanoparticles.

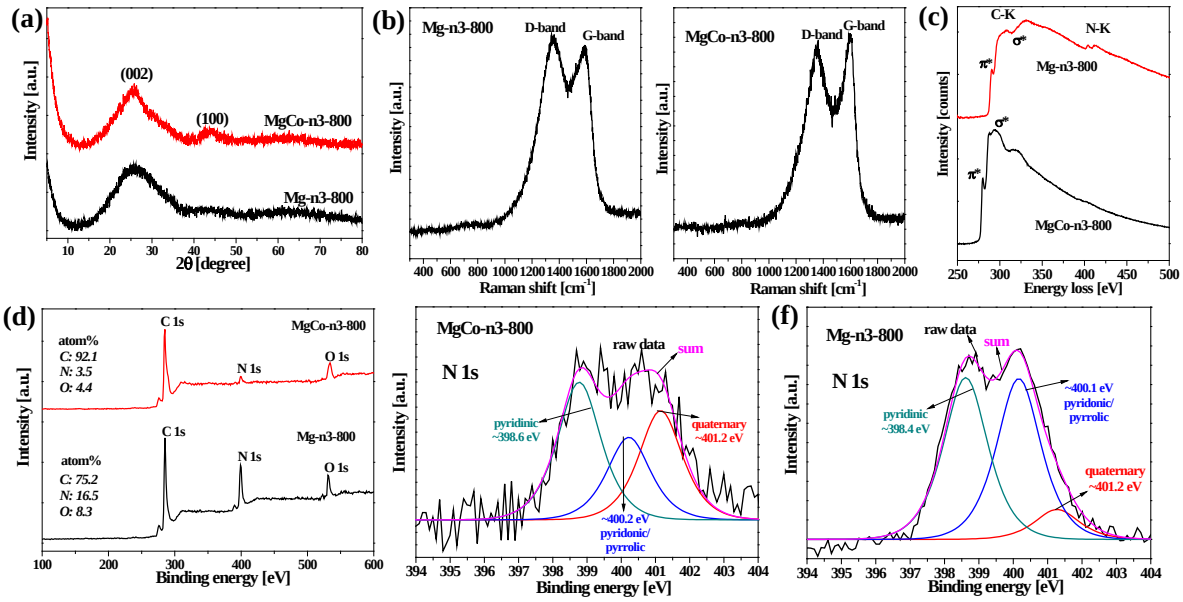

Figure 2. Structural analysis of the carbon samples calcined at 800 °C and washed with acid solution. (a) XRD patterns; b) Raman spectra; (c) TEM-EELS; (d-f) XPS.

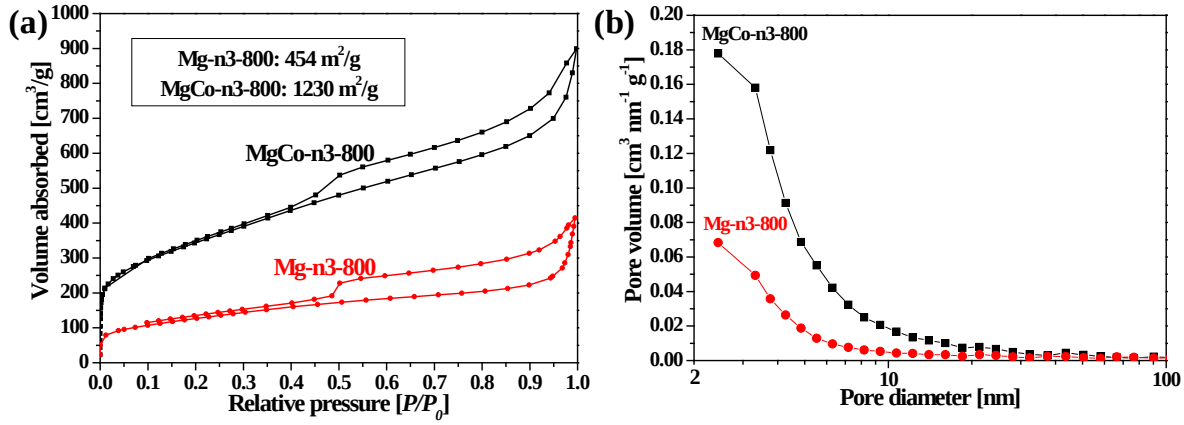

Figure 3 (a) N_2 adsorption–desorption isotherm and (b) BJH pore size distribution of the carbon samples calcined at 800 °C and washed with acid solution.

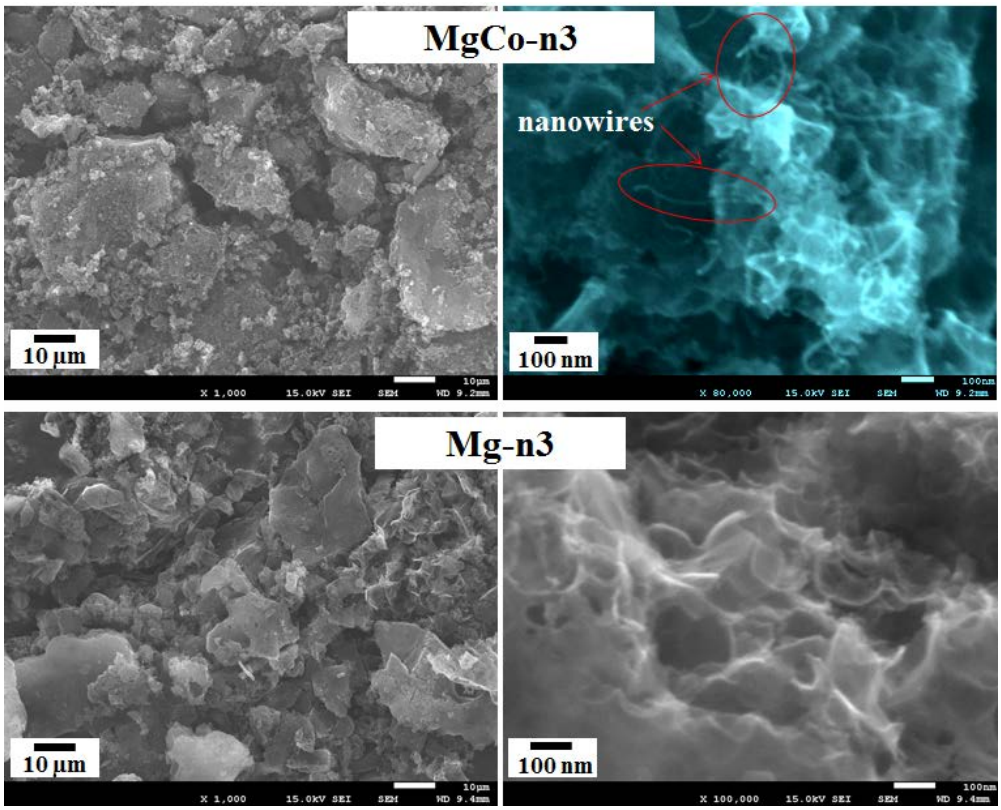

Figure 4. SEM images of the obtained carbon samples.

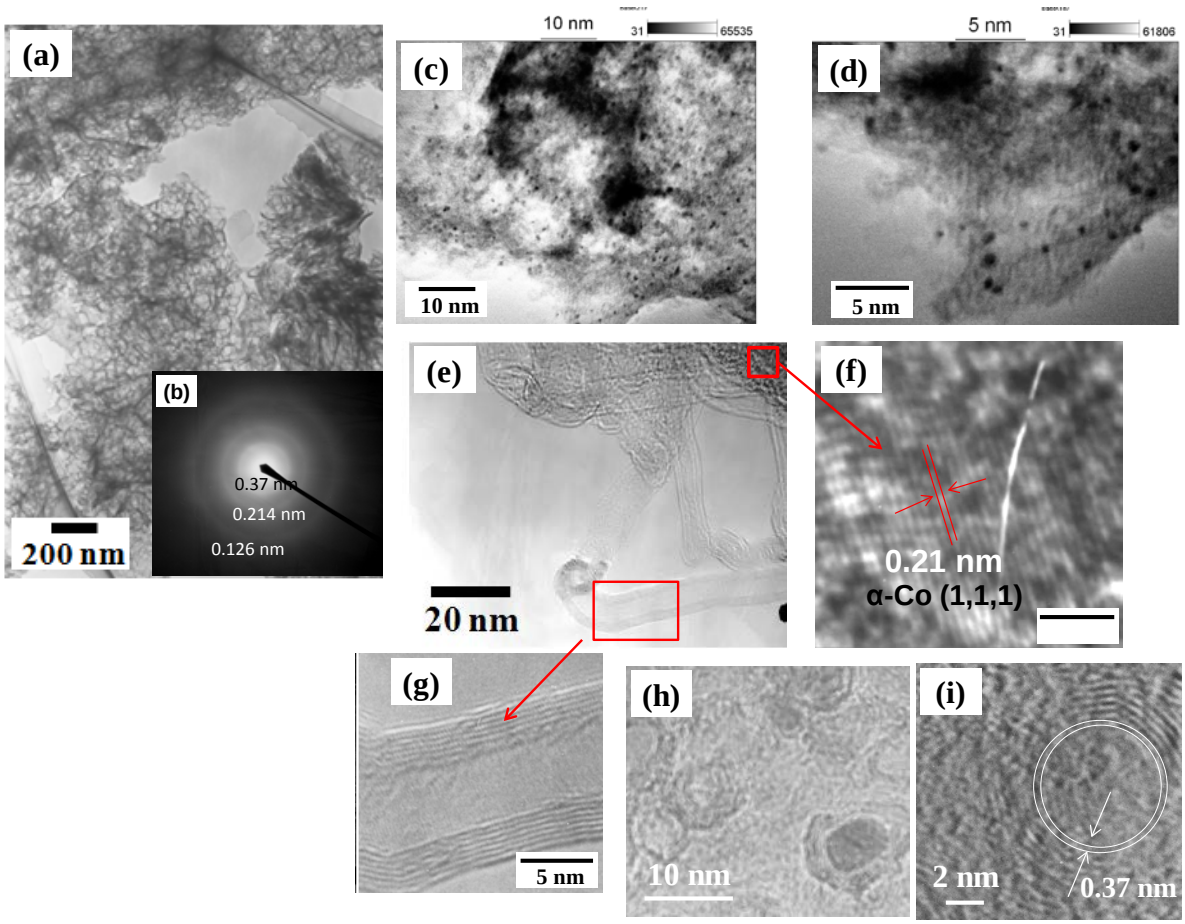

Figure 5. TEM observation for carbon sample MgCo-n3-800. (a) A typical overview TEM image at a low magnification; (b) A typical electron diffraction pattern; (c, d) HAADF images; (e, f, g) High resolution TEM images showing incorporated metallic cobalt nanoparticle and CNT; (h, i) High resolution TEM images showing incorporated metallic cobalt nanoparticles and localized graphitic layers around the etched Co nanoparticles; (j) A typical high resolution TEM image of the amorphous carbon matrix.

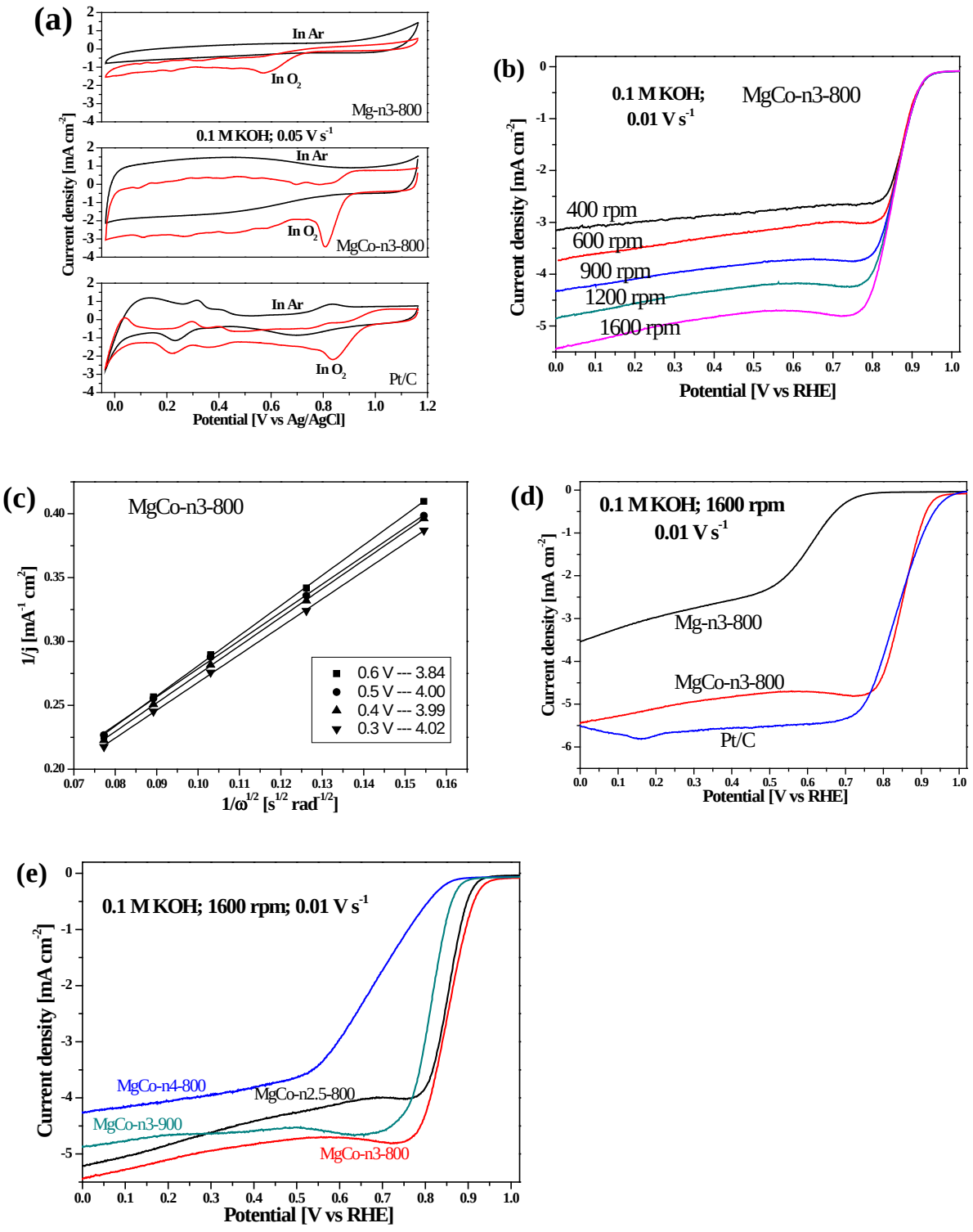

Figure 6. ORR properties of obtained carbon samples. (a) CV curves in O_2 and Ar saturated 0.1 M KOH electrolyte; (b) LSV curves for MgCo-n3-800 at various rotation rates; (c) K-L plots for MgCo-n3-800 at different potentials; (d, e) LSV curves at a rotation speed of 1600 rpm.

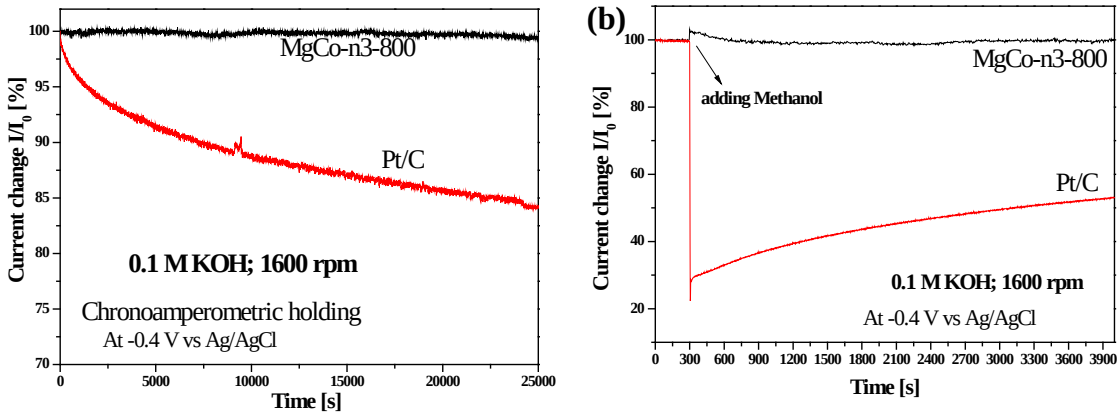

Figure 7. (a) Chronoamperometric responses and (b) methanol tolerance test of MgCo-n3-800 and Pt/C.